Effects of a Dry–Mass Conserving Dynamical Core on the Simulation of Tropical Cyclones

Shaoying LI, Jun PENG, Weimin ZHANG, Jianping WU, Qiang YAO, Xiangrong YANG, Tengling LUO

Related articles that may interest you

Ensemble Forecasts of Tropical Cyclone Track with Orthogonal Conditional Nonlinear Optimal Perturbations

Advances in Atmospheric Sciences. 2019, 36(2), 231   https://doi.org/10.1007/s00376–018–8001–1

Uncertainty in Tropical Cyclone Intensity Predictions due to Uncertainty in Initial Conditions

Advances in Atmospheric Sciences. 2020, 37(3), 278   https://doi.org/10.1007/s00376–019–9126–6

Possible Sources of Forecast Errors Generated by the Global/Regional Assimilation and Prediction System for Landfalling Tropical Cyclones. Part II: Model Uncertainty

Advances in Atmospheric Sciences. 2018, 35(10), 1277   https://doi.org/10.1007/s00376–018–7095–9

Sensitivity to Tendency Perturbations of Tropical Cyclone Short–range Intensity Forecasts Generated by WRF

Advances in Atmospheric Sciences. 2020, 37(3), 291   https://doi.org/10.1007/s00376–019–9187–6

Reduced Sensitivity of Tropical Cyclone Intensity and Size to Sea Surface Temperature in a Radiative–Convective Equilibrium Environment

Advances in Atmospheric Sciences. 2018, 35(8), 981   https://doi.org/10.1007/s00376–018–7277–5

The Simulation of Five Tropical Cyclones by Sample Optimization of Ensemble Forecasting Based on the Observed Track and Intensity

Advances in Atmospheric Sciences. 2021, 38(10), 1763   https://doi.org/10.1007/s00376–021–0353–2

AAS Website   AAS Weibo   AAS WeChat

Follow AAS public account for more information

• Original Paper •

Effects of a Dry-Mass Conserving Dynamical Core on the Simulation of Tropical Cyclones

Shaoying LI[1,2], Jun PENG[2], Weimin ZHANG[*1,2], Jianping WU[2], Qiang YAO[2],
Xiangrong YANG[2], and Tengling LUO[2]

[1]*College of Computer Science and Technology*, *National University of Defense Technology*, *Changsha* 410073, *China*
[2]*College of Meteorology and Oceanography*, *National University of Defense Technology*, *Changsha* 410073, *China*

ABSTRACT

The accurate forecasting of tropical cyclones (TCs) is a challenging task. The purpose of this study was to investigate the effects of a dry-mass conserving (DMC) hydrostatic global spectral dynamical core on TC simulation. Experiments were conducted with DMC and total (moist) mass conserving (TMC) dynamical cores. The TC forecast performance was first evaluated considering 20 TCs in the West Pacific region observed during the 2020 typhoon season. The impacts of the DMC dynamical core on forecasts of individual TCs were then estimated. The DMC dynamical core improved both the track and intensity forecasts, and the TC intensity forecast improvement was much greater than the TC track forecast improvement. Sensitivity simulations indicated that the DMC dynamical core-simulated TC intensity was stronger regardless of the forecast lead time. In the DMC dynamical core experiments, three-dimensional winds and warm and moist cores were consistently enhanced with the TC intensity. Drier air in the boundary inflow layer was found in the DMC dynamical core experiments at the early simulation times. Water vapor mixing ratio budget analysis indicated that this mainly depended on the simulated vertical velocity. Higher updraft above the boundary layer yielded a drier boundary layer, resulting in surface latent heat flux (SLHF) enhancement, the major energy source of TC intensification. The higher DMC dynamical core-simulated updraft in the inner core caused a higher net surface rain rate, producing higher net internal atmospheric diabatic heating and increasing the TC intensity. These results indicate that the stronger DMC dynamical core-simulated TCs are mainly related to the higher DMC vertical velocity.

Key words: dry mass conservation, tropical cyclone, intensity forecast, track forecast

Article Highlights:

• Both the predicted TC tracks and intensities are improved with the DMC dynamical core.
• The improvement in the TC intensity forecasts is much greater than that in the TC track forecasts.
• The TC intensity obtained with the DMC dynamical core is stronger, which is mainly related to the simulated vertical velocity.

---

1. Introduction

The accurate forecasting of tropical cyclones (TCs) is a challenging task (Cangialosi et al., 2020; Rogers, 2021). Over the last decades, numerical forecasting of TC tracks has attained notable progress. However, little progress has been achieved in TC intensity forecasting (Emanuel, 2000; Emanuel et al., 2004; Sun et al., 2019; Cangialosi et al., 2020; Schaffer et al., 2020). The difficulties in predicting TC intensity can be attributed to its complexity. TC intensity variation can be affected by various external processes [e.g., sea surface temperature (SST) and environmental vertical shear] and internal processes (e.g., spiral rainbands and surface heat fluxes) (Vigh, 2018; Hendricks et al., 2019; Tang et al., 2020). However, the conversion between water categories in the above spiral rainbands is very important because this phenomenon is related to mass continuity, pressure tendency, and vertical velocity equations (Gu and Qian, 1991; Qiu et al., 1993; Lackmann and Yablonsky, 2004). But they are neglected in most global numerical models (Neale et al., 2012; Wedi et al., 2015).

---

* Corresponding author: Weimin ZHANG
  Email: wmzhang104@139.com

A reasonable approximation of the governing equations of numerical modeling systems constitutes a vital step to ensure the accuracy of the TC intensity forecasting for numerical models (Rogers, 2021). Since the governing equations of models are approximations of actual physical laws, these approximate equations can limit the predicted phenomena (Lorenz, 1960; Byun, 1999; Dudhia, 2014; Bauer et al., 2015). In most global models, such as the Integrated Forecast System (IFS) developed by the European Centre for Medium-Range Weather Forecasts (ECMWF) (Wedi et al., 2015) and the Community Atmosphere Model (CAM) of the National Center for Atmospheric Research (NCAR) (Neale et al., 2012), the mass of the total moist air is assumed to be conserved in the derivation of the mass continuity equation. As a result, pressure tendency, mass continuity, and full pressure vertical velocity equations do not consider the effects of the addition or removal of moist species when there is precipitation or evaporation. However, Gu and Qian (1991) proposed that precipitation mass sinks cannot be overlooked in heavily precipitating systems. Qiu et al. (1993) and Lackmann and Yablonsky (2004) suggested that the addition or removal of water vapor resulting from evaporation or precipitation could considerably influence the TC dynamics, resulting in a stronger TC intensity characterized by heavier precipitation. Moreover, the physical processes associated with hydrometeor production and conversion in rainbands could significantly affect TC structure and intensity changes (Wang, 2009; Li and Wang, 2012; Li et al., 2014; Vigh, 2018; Hendricks et al., 2019; Tang et al., 2020). Diabatic heating (cooling) in inner rainbands, the region within a radius of approximately 2–3 times the radius of maximum wind (RMW) (Wang, 2009), could increase (decrease) the TC intensity (Li et al., 2014). Evaporation in inner rainbands exerts negligible effects on TC intensity variation, while evaporation in outer rainbands leads to less intense TCs (Li et al., 2015). It could be that the effect of an inaccurate description of the vertical velocity in the precipitation area leading to convective heating in inner rainbands is limited, which may be one of the reasons why the intensity of strong TCs is underestimated (Yan et al., 2016; Bloemendaal et al., 2019). In addition, total-moist air conservation could result in false compensation by a sink (source) of dry air upon evaporation (precipitation) occurrence (Bott, 2008; Lauritzen et al., 2018; Malardel et al., 2019; Peng et al., 2020).

Recently, Peng et al. (2020) developed a dry-mass conserving (DMC) hydrostatic global spectral dynamical core in a general moist atmosphere. After rigorous derivation based on inherent mass conservation of dry air, the pressure tendency, full continuity and full pressure vertical velocity equations all considered the effect of water vapor addition or removal. Then, they conducted an idealized TC experiment, which revealed that the TC-like storms simulated with the DMC dynamical core were more intense, compact, and concentric and much more in line with the results of other global models. However, they did not evaluate the impact of the DMC dynamical core on numerical forecasts

considering real TC cases nor did they provide a complete physical explanation for why the TC simulated by the DMC dynamical core is stronger. Thus, this study is aimed to verify the above finding based on observed TCs and formulate a possible explanation.

Given the high potential of the DMC dynamical core to enhance the TC intensity forecast skill, it is of great interest to explore the mechanism of the possible improvements in DMC-aided TC intensity forecasts. This paper is organized as follows: Section 2 describes the DMC and the total (moist) mass conserving (TMC) dynamical cores and presents an overview of the experimental configurations. Statistics are given in section 3. Section 4 provides a case analysis, including a brief description of the case and experiments, and interprets the numerical simulation results. Finally, conclusions and a discussion are contained in section 5.

2. Dynamical cores and experimental configurations

2.1. *DMC dynamical core*

The DMC dynamical core employed in this paper was developed by Peng et al. (2019, 2020), and the following description of the DMC dynamical core is derived from the aforementioned study with minor modifications. To ensure that the dry air mass is conserved, the DMC hydrostatic global spectral dynamical core was developed in dry-mass vertical coordinates (η_d-coordinates, i.e., hybrid terrain-following coordinates based on the dry hydrostatic pressure). The mass continuity equation for the dry air density can be expressed as follows:

$$\frac{\partial}{\partial t}\left(\frac{\partial \pi_d}{\partial \eta_d}\right) + \nabla \cdot \left(\frac{\partial \pi_d}{\partial \eta_d}\boldsymbol{u}\right) + \frac{\partial}{\partial \eta_d}\left(\frac{\partial \pi_d}{\partial \eta_d}\frac{d\eta_d}{dt}\right) = 0 \,, \qquad (1)$$

where π_d is the dry hydrostatic pressure and $\boldsymbol{u}$ is the horizontal wind vector.

After integrating the above mass continuity equation [Eq. (1)] from the atmosphere top ($\eta_d = 0$) to the surface ($\eta_d = 1$), the tendency equation of the surface dry hydrostatic pressure π_{ds} can be obtained as follows:

$$\frac{\partial \pi_{ds}}{\partial t} = -\int_0^1 \nabla \cdot \left(\frac{\partial \pi_d}{\partial \eta_d}\boldsymbol{u}\right) d\eta_d \,. \qquad (2)$$

The full pressure vertical velocity $\omega(\eta_d)$ in dry-mass vertical coordinates can be rigorously derived as follows:

$$\omega(\eta_d) = \frac{d\pi_d}{dt} + \int_0^{\eta_d}\left(-q_t\frac{\partial \pi_d}{\partial \eta_d}\nabla \cdot \boldsymbol{u}\right)d\eta_d +$$
$$\int_0^{\eta_d}\left(\frac{\partial \boldsymbol{u}}{\partial \eta_d}\cdot\nabla\frac{\partial \pi_d}{\partial \eta_d}\right)d\eta_d +$$
$$\int_0^{\eta_d}\frac{\partial \pi_d}{\partial \eta_d}\left(\frac{dq_t}{dt}\right)d\eta_d \,, \qquad (3)$$

where $q_t = q_v + q_c + q_r + \cdots$ and the subscripts t, v, c, and r denote the total mixing ratio, water vapor mixing ratio, cloud water mixing ratio, and rainwater mixing ratio, respectively, for any constituent other than dry air. Please refer to Peng et al. (2019, 2020) for more details.

2.2. TMC dynamical core

If the total mass is conserved, according to Malardel et al. (2019), the continuity equation in moist-air vertical coordinates (η-coordinates) can be written as follows:

$$\frac{\partial}{\partial t}\left(\frac{\partial \pi}{\partial \eta}\right) + \nabla \cdot \left(\frac{\partial \pi}{\partial \eta}\boldsymbol{u}\right) + \frac{\partial}{\partial \eta}\left(\dot{\eta}\frac{\partial \pi}{\partial \eta}\right) = 0 , \qquad (4)$$

where π is the moist hydrostatic pressure and $\dot{\eta} = \mathrm{d}\eta/\mathrm{d}t$ is the generalized vertical velocity. The corresponding tendency equation for the surface moist hydrostatic pressure π_s is:

$$\frac{\partial \pi_s}{\partial t} = -\int_0^1 \nabla \cdot \left(\frac{\partial \pi}{\partial \eta}\boldsymbol{u}\right)\mathrm{d}\eta . \qquad (5)$$

The full pressure vertical velocity $\omega(\eta)$ can be calculated as follows:

$$\omega(\eta) = \frac{\mathrm{d}\pi}{\mathrm{d}t} = -\int_0^\eta \nabla \cdot \left(\frac{\partial \pi}{\partial \eta}\boldsymbol{u}\right)\mathrm{d}\eta + \boldsymbol{u}\cdot\nabla\pi . \qquad (6)$$

2.3. Difference between the DMC and TMC dynamical cores

As reported in Malardel et al. (2019), if we assure that dry air is conserved in η-coordinates, the above continuity equation [Eq. (4)] can be rewritten as follows:

$$\frac{\partial}{\partial t}\left(\frac{\partial \pi}{\partial \eta}\right) + \nabla \cdot \left(\frac{\partial \pi}{\partial \eta}\boldsymbol{u}\right) + \frac{\partial}{\partial \eta}\left(\dot{\eta}\frac{\partial \pi}{\partial \eta}\right) = \frac{\partial \pi}{\partial \eta}S_w , \qquad (7)$$

where S_w is the change in the total water.

The surface pressure tendency equation [Eq. (5)] can be rewritten as follows:

$$\frac{\partial \pi_s}{\partial t} = -\int_0^1 \nabla \cdot \left(\frac{\partial \pi}{\partial \eta}\boldsymbol{u}\right)\mathrm{d}\eta + \int_0^{\pi_s} S_w\mathrm{d}\pi . \qquad (8)$$

The full pressure vertical velocity equation [Eq. (6)] can be rewritten as follows:

$$\omega(\eta) = -\int_0^\eta \nabla \cdot \left(\frac{\partial \pi}{\partial \eta}\boldsymbol{u}\right)\mathrm{d}\eta + \boldsymbol{u}\cdot\nabla\pi + \int_0^\pi S_w\mathrm{d}\pi . \qquad (9)$$

The obvious differences between the DMC and TMC dynamical cores are that the change in the total water is considered in the continuity equation, surface pressure tendency equation and full pressure vertical velocity equation.

2.4. Experimental configurations

The Yin-He Global Spectral Model (YHGSM; Wu et al., 2011; Yang et al., 2017; Yin et al., 2018, 2021) developed by the College of Meteorology and Oceanography at the National University of Defense Technology (NUDT) was employed in this study. Originally, the dynamical core employed in the YHGSM is a TMC hydrostatic core. Based on the work of Peng et al. (2019, 2020), the DMC hydrostatic global spectral dynamical core was applied in the YHGSM. To illustrate the effect of the DMC dynamical core on TC forecasts, numerical simulations using the DMC and TMC dynamical cores were conducted with the same physics package, including Weather Research and Forecasting (WRF) single-moment 5-class (WSM5) scheme (Hong et al., 2004) updated with an additional prognostic equation of the cloud fraction (Forbes et al., 2011; Forbes and Tompkins, 2011), new Tiedtke cumulus parameterization scheme (Zhang and Wang, 2017), the rapid radiative transfer model for general circulation model applications (Mlawer et al., 1997; Iacono et al., 2008), and University of Washington turbulent kinetic energy (or TKE) boundary layer scheme (Bretherton and Park, 2009). The same initial conditions retrieved from YHGSM analysis data were used to reduce the impacts of initial conditions on TC forecasting (Wang et al., 2020). A $T_L 1279 L137$ resolution was used, and the integration time step was $\Delta t = 600$ s. The SST was maintained constant during model integration.

3. Statistics

To assess the overall performance of the DMC dynamical core in TC track and intensity forecasting, TC track and intensity forecasts were evaluated for all 20 TCs observed in the West Pacific region during the 2020 typhoon season (1 May to 31 October) in each of the three intensity classifications. Here, the TC center along the track was determined with the Geophysical Fluid Dynamics Laboratory (GFDL) Vortex Tracker (Marchok, 2021) (GFDL-VT). Please refer to the user manual for additional details (Biswas et al., 2018). Best track data were obtained from the Shanghai Typhoon Institute of the China Meteorological Administration (CMA; https://tcdata.typhoon.org.cn/zjljsjj_zlhq.html; Ying et al., 2014; Lu et al., 2021). TC simulations initialized at 0000 UTC at 24-h intervals were included in the statistics. The mean TC track and intensity forecast errors are shown in Fig. 1. In regard to the mean overall TC track errors, the mean overall forecast errors of the DMC dynamical core were slightly smaller than those of the TMC dynamical core at most forecast times, with an overall TC track forecast error reduction of no more than 4% over the 24–72-h forecast periods and 6%–7% over the 96–120-h forecast periods (Fig. 1a1). In terms of the mean overall intensity forecast errors, notably lower biases were observed for the DMC dynamical core than for the TMC dynamical core at all forecast times, with the smallest reduction of 17% at 96 h and the largest reduction of 35% at 120 h (Fig. 1a2). Regarding the track errors in the three intensity classifications, the track errors were similar to the mean overall track error over the 24–96-h forecast periods, i. e., the track errors of the DMC dynamical core were slightly smaller (or slightly larger) than those of the TMC dynamical core, except for the greatest deterioration (improvement) of

18.5% (20.7%) in the tropical storm (typhoon) intensity at 120 h. In terms of the intensity errors in the three intensity classifications, the DMC dynamical core typically achieved an improvement with the largest reduction of 52.6% at
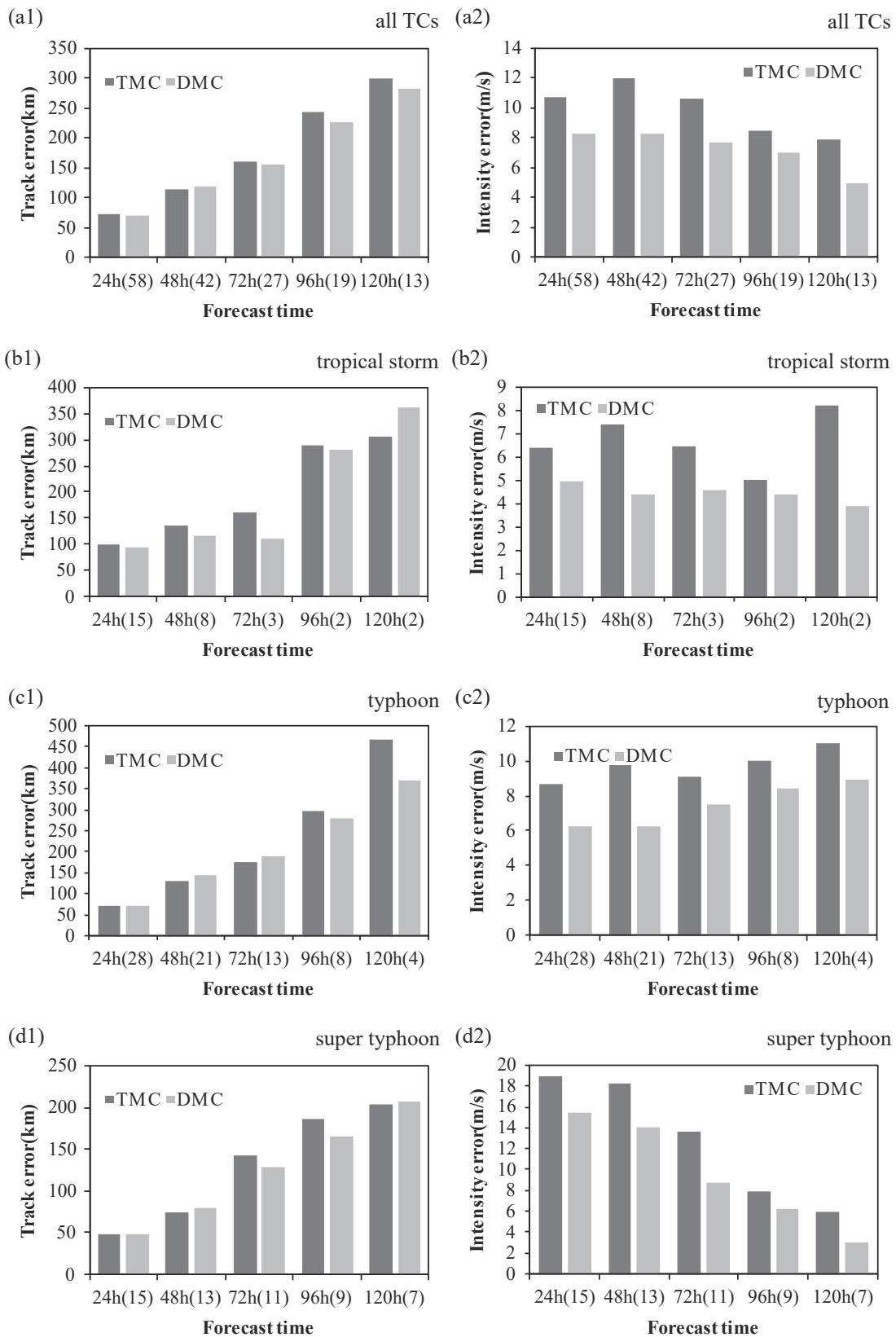

Fig. 1. Track forecast errors (km) and intensity forecast errors (m s^{-1}) for all TCs and the different TC intensity categories averaged over the 2020 typhoon season (1 May to 31 October) in the West Pacific region. The sample sizes are shown in parentheses next to the time.

120 h and the smallest reduction of 12.8% at 96 h in the tropical storm intensity. In general, the DMC dynamical core attained satisfactory prediction ability regarding TC track and intensity, and the DMC dynamical core performed much better in terms of the predicted intensity than the predicted TC track.

4. Case analysis

4.1. *Super Typhoon Maysak (2020) and experiments*

4.1.1. *Super Typhoon Maysak (2020)*

To better understand the impacts of the DMC dynamical core on TC position and intensity forecasting, an individual TC case was analyzed. As such, Super Typhoon Maysak (2020) was chosen. Maysak (2020) originated east of Luzon Island in the Philippines and was categorized as a TC at approximately 0700 UTC on 28 August 2020. After 0300 UTC on 29 August 2020, Maysak (2020) moved northward and gradually intensified. At approximately 2100 UTC on 31 August, Maysak (2020) reached its strongest state with a central sea level pressure (SLP) of 930 hPa and a maximum wind speed of 52 m s^{-1} and was categorized as a super typhoon by the CMA. Subsequently, Maysak (2020) moved northeastward and weakened to a certain degree. Later, this TC made landfall on the coast of South Kyongsang Province, South Korea, at approximately 1730 UTC on 2 September with a maximum wind speed of 42 m s^{-1} and then continued northward to enter Jilin Province, China, at 0540 UTC on 3 September. Maysak (2020) caused at least 1 death and 19 injuries.

4.1.2. *Numerical experiments*

Two simulations, denoted as DMC (using the DMC dynamical core) and TMC (using the TMC dynamical core), were initiated at 0000 UTC on 30 August 2020. Several sensitivity experiments, including the aforementioned DMC and TMC experiments, are summarized in Table 1. The simulations which initialized at 0000 UTC on 29 August 2020 and continued to 0000 UTC on 31 August 2020 at 24-h intervals were considered to examine the sensitivity of the numerical simulation results to the forecast lead time.

4.2. *Maysak (2020) track and intensity simulations*

The simulated track and intensity of Maysak (2020) with the DMC dynamical core (solid colored lines) and

TMC dynamical core (dashed colored lines) for different forecast lead times were compared to the acquired TC best track data (solid black lines), as shown in Fig. 2. Overall, the general track evolution behavior is reasonably simulated with both the DMC and TMC dynamical cores. The DMC simulation experiment more consistently yielded suitable track predictions than those obtained in the TMC simulation experiment. However, the simulated tracks retrieved from both the DMC-24 h and TMC-24 h experiments with an early initialization time exhibited an eastern bias during most of the simulation period, even though the track errors of the DMC-24 h experiment were smaller than those of the TMC-24 h experiment. The tracks indicated no remarkable differences between the DMC+24 h and TMC+24 h experiments with no obvious bias during most of the simulation period compared to the best track data, even for the later forecast lead time (not given). Consequently, the DMC dynamical core outperformed the TMC dynamical core in numerically simulating the Maysak (2020) track.

In contrast, in terms of the intensity of Maysak (2020), there were no obvious differences during the first few hours. The largest difference between the DMC and TMC dynamical cores is the change in total water in the continuity equation, and Eq. (9) includes an additional term associated with the total water; consequently, the initial vortex obtained with the DMC scheme spins up more rapidly than that obtained with the TMC scheme. Therefore, upon TC intensification, the differences between the DMC and TMC dynamical cores become increasingly significant. And landfalling TCs were sharply weakened in the DMC experiments. The TMC dynamical core produced much lower intensities of the minimum SLP and near-surface wind speed than those produced by the DMC dynamical core in all numerical simulations (Fig.2). These results confirmed the conclusions based on the above earlier idealized TC test (Peng et al., 2020). Although three simulations using the DMC dynamical core generated more intense TCs than the observations at approximately 1200 UTC 2 September (Fig. 2), which may be a result of the higher SST (not shown), they all successfully capture the evolution of the TC intensity. Overall, compared to the TMC dynamical core, the DMC dynamical core produced better simulation results in terms of the TC track and intensity. The above results indicate that the DMC dynamical core is important in model development for TC forecasting purposes, especially to improve the TC intensity forecasting skill, which is consistent with the statistical conclusions.

Table 1. Model configurations for the numerical simulation experiments.

Experiments	Dynamical core	Simulation period
DMC-24 h	DMC dynamical core	0000 UTC 29 Aug–0000 UTC 4 Sep
TMC-24 h	TMC dynamical core	0000 UTC 29 Aug–0000 UTC 4 Sep
DMC	DMC dynamical core	0000 UTC 30 Aug–0000 UTC 4 Sep
TMC	TMC dynamical core	0000 UTC 30 Aug–0000 UTC 4 Sep
DMC+24 h	DMC dynamical core	0000 UTC 31 Aug–0000 UTC 4 Sep
TMC+24 h	TMC dynamical core	0000 UTC 31 Aug–0000 UTC 4 Sep

4.3. Structure of the simulated TCs

The above sensitivity experiments indicated that regardless of the forecast lead time, the DMC dynamical core could improve strong TC intensity forecasts by producing
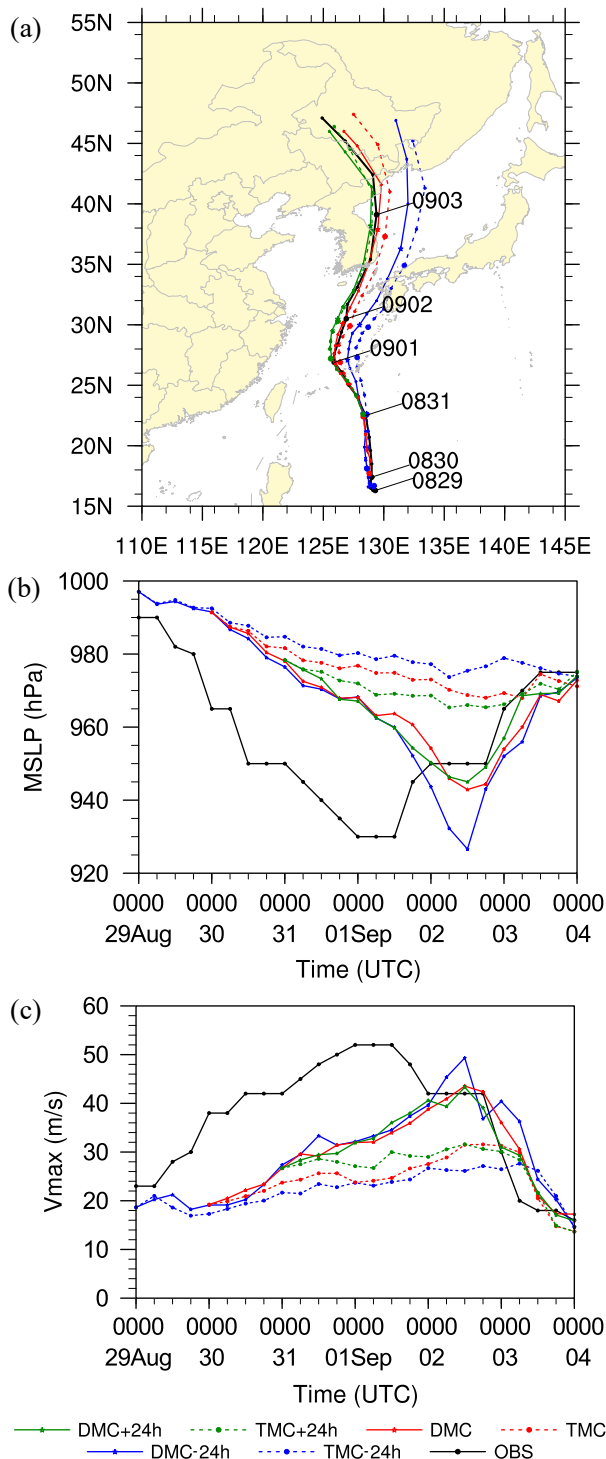

Fig. 2. (a) Observed best tracks (black) retrieved from the CMA and simulated tracks obtained with the DMC (solid colored lines) and TMC (dashed colored lines) dynamical cores of Typhoon Maysak (2020) starting at different times, (b) similar to (a) but for the minimum sea level pressure (hPa), and (c) similar to (b) but for the maximum surface winds (m s⁻¹).

much more intense TCs. To interpret the improvement in TC intensity forecasts with the DMC dynamical core, the differences between the DMC and TMC simulation experiments, covering the period of Maysak (2020) intensification and development, were investigated. Therefore, the DMC and TMC simulation experiments were further compared.

Figure 3 shows snapshot plan views of the mean SLP and 10-m surface winds at 12 h, 42 h, and 84 h. At 12 h, the mean SLP did not notably differ between the DMC and TMC experiments, but a slightly higher 10-m surface wind speed with a slightly intense upward motion (Fig. 4) occurred in the area north of the TC in the DMC simulation. Over time, these differences increased until the largest values were reached at 84 h. At 84 h, both simulations attained their strongest state, but the DMC simulation yielded a much lower mean SLP (Figs. 3c1–c2), much higher 10-m surface wind speed (Figs. 3c1–c2), and much more intense upward motions than those obtained in the TMC simulation (Figs. 4c1–c2).

Height–radial plots of the azimuthally averaged winds at 84 h are shown in Fig. 5. By determining three-dimensional winds (Fig. 5), both simulations were shown to capture the typical structures of real TCs: radial outflow at the upper level, radial inflow at the lower level, and slantwise upward motion. The slantwise upward motion with an average peak intensity of 6 hPa s⁻¹ at 710 hPa in the DMC simulation was obviously stronger than that in the TMC simulation with an average peak intensity of 2 hPa s⁻¹ at 850 hPa. In the DMC simulation, stronger outflow occurred in the upper troposphere and was more evident than the low-level radial inflow. The maximum tangential velocity in the DMC simulation at approximately 1 km above the surface was higher than that in the TMC simulation, and the radius of the maximum tangential velocity was smaller.

Figure 6 shows time–height Hovmöller plots of the azimuthally and radially averaged perturbation temperature. The mean temperature averaged over the 550–650-km annulus was defined as the environmental temperature, similar to Stern and Nolan (2012). In both experiments, the perturbation temperature was the highest from 400–250 hPa (8–10 km), but the height of the middle-level maximum perturbation temperature did not vary much except for lowering to approximately 400 hPa (7 km) from 96–108 h. In addition to this primary maximum, a low-level maximum and a third maximum were found in the DMC experiment at 600 hPa (4 km) during the simulation period and below 900 hPa after 12 h, respectively, while these second and third maxima occurred in the TMC experiment after approximately 48 h. However, the height of the warm core did not correspond to the TC intensity (Stern and Nolan, 2012), but the strength of the warm core was generally well-correlated with the TC intensity (Ma et al., 2013). During the TC intensification period (0–84 h), the warm cores steadily strengthened over time, and the warm cores in the DMC simulation were notably stronger than those in the TMC simulation for all middle and low-level maxima.

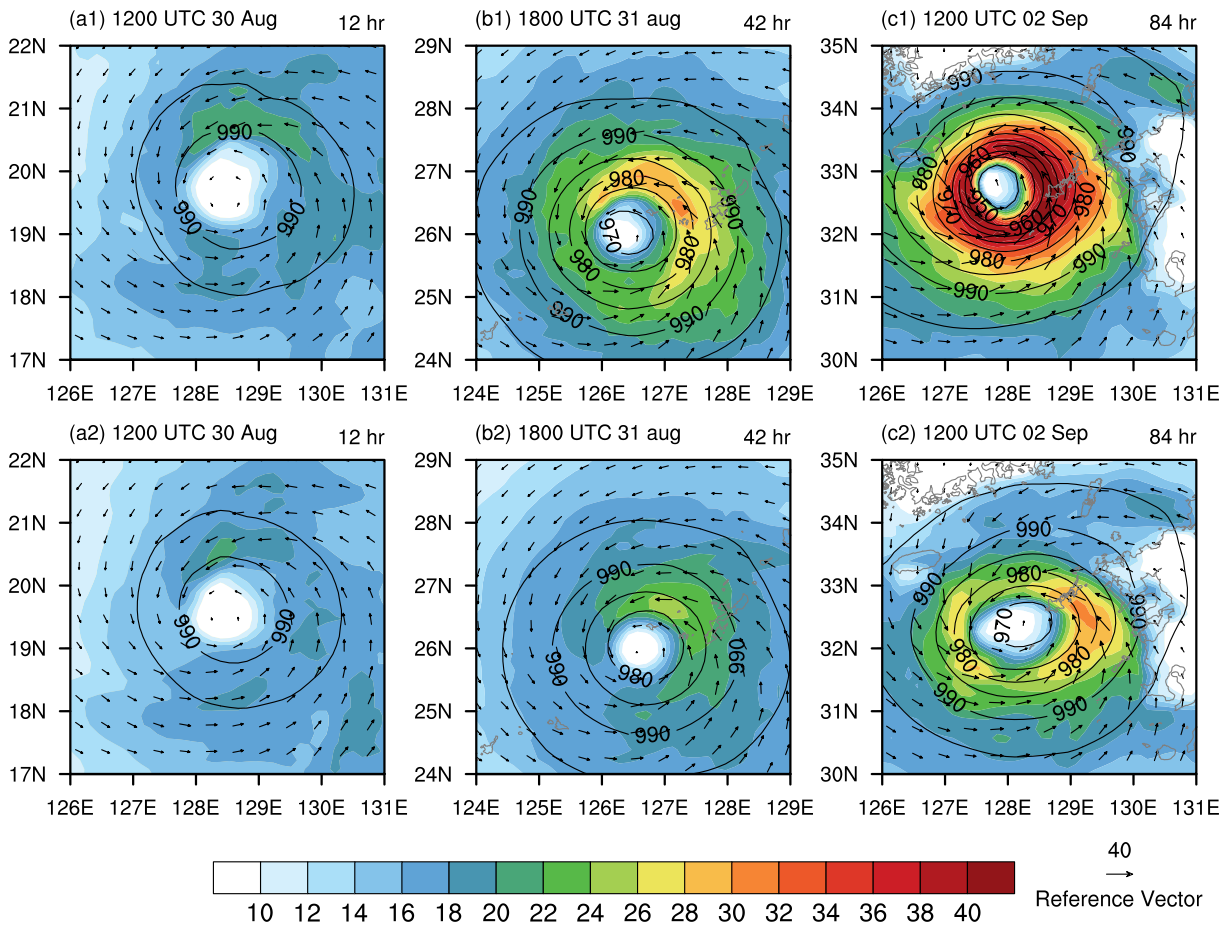The equivalent potential temperature (EPT, θ_e), derived

Fig. 3. Plan views of the mean sea level pressure (contour, 5 hPa) and 10-m surface winds (m s⁻¹, the shading indicates the wind speed, and the vectors indicate the wind direction) at 12 h (a1, a2), 42 h (b1, b2), and 84 h (c1, c2) in the (a1, c1) DMC and (a2, c2) TMC simulations.

from the first law of thermodynamics and exhibiting conservation properties, attains a close relationship with TC evolution (Ma et al., 2013). Following Bolton (1980), the EPT can be obtained as follows:

$$\theta_e \approx \theta \exp\left[\left(\frac{3.376}{T_L} - 0.00254\right) \times q(1 + 0.00081q)\right], \quad (10)$$

where θ is the potential temperature and T_L and q are the lifted temperature and water vapor mixing ratio, respectively. Figure 7 shows height–radius cross sections of the EPT at different times in the DMC (Figs. 7a1–d1) and DMC–TMC simulation experiments (Figs. 7a2–d2). The EPT steadily increased over time, and the altitude of the higher EPT value in the DMC simulation, compared to that in TMC simulation, at the storm center deepened over time. Notably, in the boundary layer, the EPT in the DMC simulation was lower than that in the TMC simulation within a radius of more than 50 km at earlier times (Fig. 7a2), indicating that the energy in the boundary layer in the DMC simulation was lower than that in the TMC simulation. The difference in the EPT (Figs. 7a2–d2) was similar to the difference in the water vapor mixing ratio (Figs. 7a4–d4). This finding indicated that the change in the EPT was mainly determined

by moist processes. The early lower EPT in the boundary layer in the DMC simulation (Fig. 7a2) was mainly caused by the lower water vapor mixing ratio in the boundary layer (Fig. 7a4).

The temporally and azimuthally averaged temperature difference between the DMC and TMC simulation at the different times (Figs. 7a3–d3) and the water vapor mixing ratio difference (Figs. 7a4–d4) are also shown in Fig. 7. At 6 h, there occurred a distinctly positive temperature difference centered at an altitude of 600 hPa with a radius of 110 km from the TC center. The warm core heights in the DMC and TMC simulations reached 330 hPa and 600 hPa at this time (Fig. 6). Corresponding to the temperature difference, at a height of 950 hPa in the storm center, there existed a moist core center. The upper level at the storm center was drier. The warmer and moister cores in the DMC simulation deepened over time, which was beneficial to TC development. It should be noted that there occurred a much drier boundary inflow layer in the DMC simulation at earlier times, which did not seem beneficial for supplying moisture to the upper eyewall region.

The surface latent heat flux (SLHF) is the major energy source of TC intensification (Wang and Xu, 2010; Ma et al., 2015). The SLHF can be computed as follows:
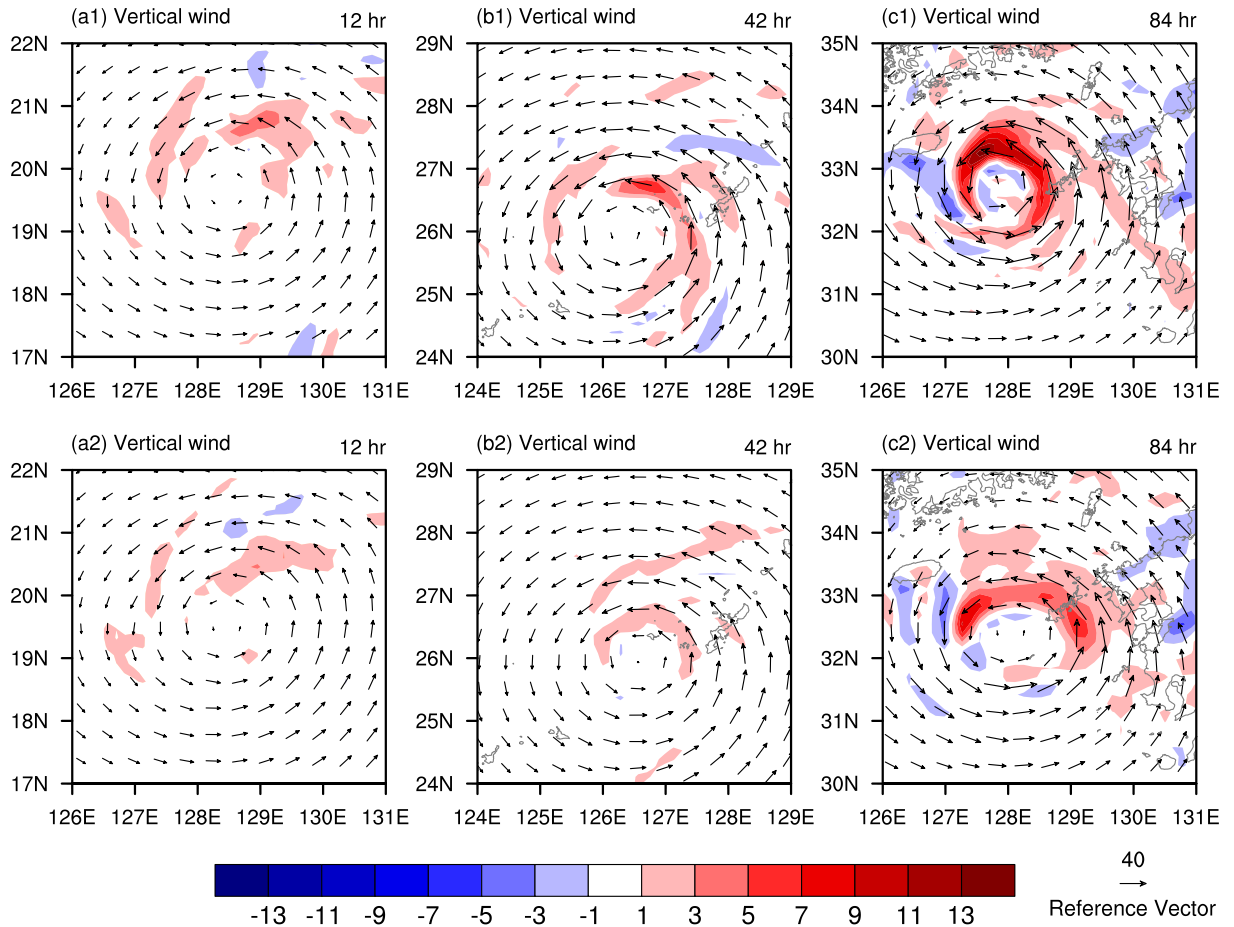
Fig. 4. Same as in Fig. 3 but for the horizontal (vectors, m s^{-1}) and vertical winds (shaded, hPa s^{-1}) at 850 hPa; the positive values denote updrafts.
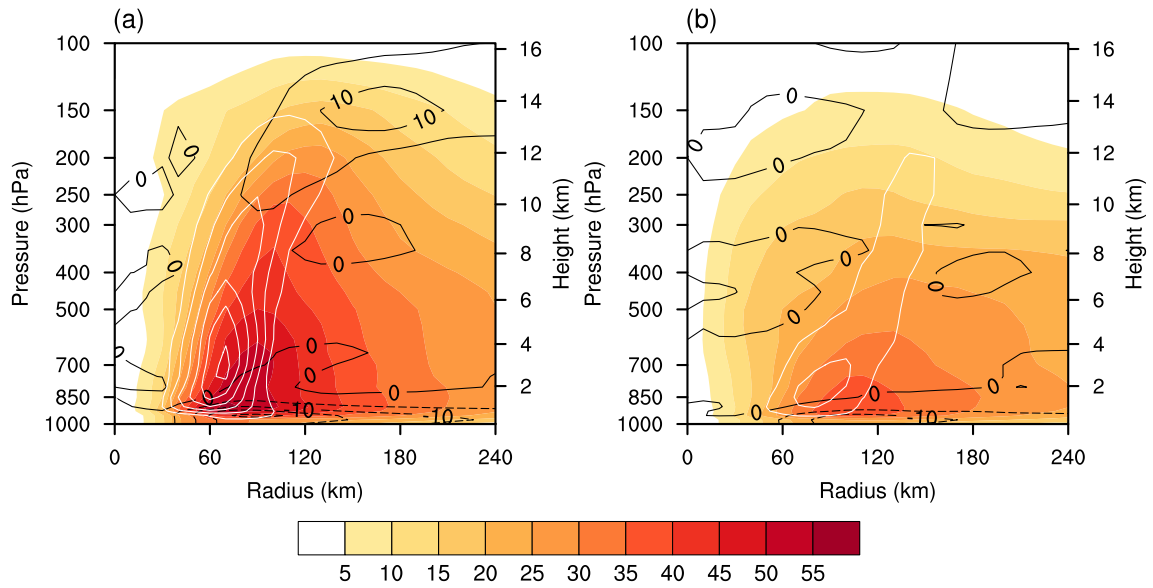

Fig. 5. Height–radius cross sections of the azimuthal-mean tangential winds (shaded; m s^{-1}), radial winds (black contours; m s^{-1}), and vertical winds (white contours; hPa s^{-1}) at 84 h in the DMC (a) and TMC simulations (b). The vertical winds are shown at contour intervals of 1 hPa s^{-1} with a minimum value of 1.

$$\text{SLHF} = \rho L_{\mathrm{v}} C_{\mathrm{q}} U_{\mathrm{a}} (q_{\mathrm{s}} - q_{\mathrm{a}}) = \rho L_{\mathrm{v}} C_{\mathrm{q}} U_{\mathrm{a}} \Delta q \,, \qquad (11)$$

where ρ is the air density in the surface layer, L_{v} is the

latent heat of vaporization, C_{q} is the surface exchange coefficient for moisture, U_{a} is the horizontal wind speed at the low-
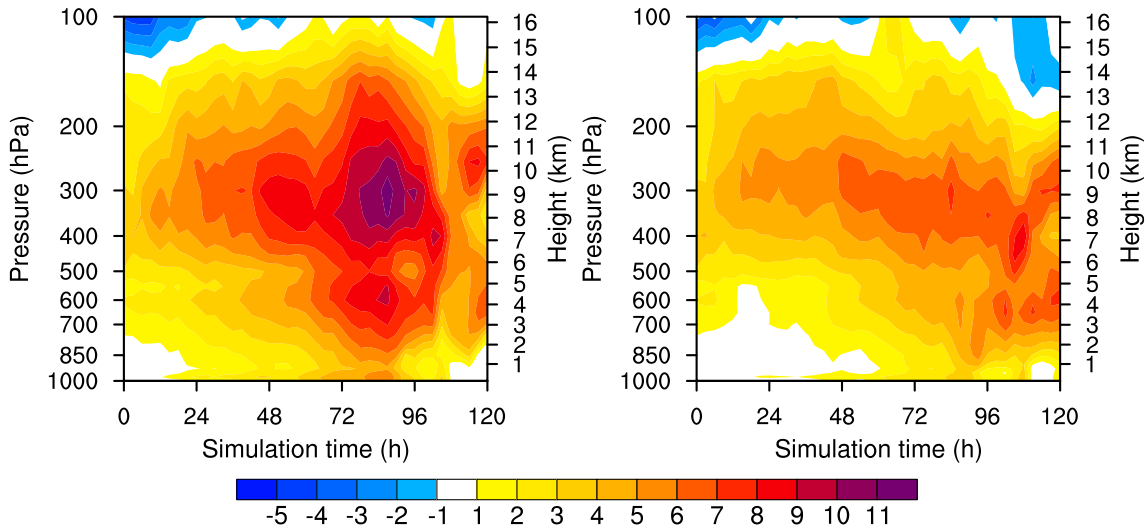
Fig. 6. Time–height Hovmöller plots of the azimuthally and radially averaged perturbation temperature (K) within a radius of 60 km from the TC center in the (a) DMC and (b) TMC simulations.

est model level, $\Delta q = q_s - q_a$, and q_s and q_a are the water vapor saturation mixing ratio at the SST and the water vapor mixing ratio at the lowest model level, respectively. The obtained SLHFs are shown in Fig. 8. Without ocean feedback, the SST remained constant and the same in both simulations. According to Eq. (11), although there occurred a much drier boundary inflow layer in the DMC simulation at earlier times, this resulted in a higher SLHF. The temporal variation in the SLHF demonstrated that the DMC simulation yielded higher SLHFs than those obtained in the TMC simulation and considerably higher values than those obtained in the TMC simulation after 48 h, which contributed to the DMC simulation producing a stronger TC than the TMC simulation.

4.4. *Budget of the water vapor mixing ratio*

At early times, the air at altitudes from 900 hPa to 300 hPa in the eye region and the air in the boundary inflow layer were distinctly drier, while the air at altitudes from 950 hPa to 500 hPa in the eyewall region, located just below the height of the warm core, became moister in the DMC simulation. At later times, the air in the DMC simulation was warmer and moister than that in the TMC simulation. To determine the reason for the water vapor mixing ratio differences between the DMC and TMC simulations, the azimuthal-mean tangential water vapor mixing ratio budget equation was further analyzed and the budget equation can be written as follows (Ma et al., 2013):

$$\frac{\partial \overline{q_v}}{\partial t} = \left(-\bar{u}\frac{\overline{\partial q_v}}{\partial r}\right) + \left(-\bar{w}\frac{\overline{\partial q_v}}{\partial z}\right) +$$
$$\left[-\left(\overline{u'\frac{\partial q'_v}{\partial r}} - \overline{\frac{v'}{r}\frac{\partial q'_v}{\partial \lambda}} - \overline{w'\frac{\partial q'_v}{\partial z}}\right)\right] +$$
$$(\bar{E} - \bar{C} + \bar{F}). \tag{12}$$

The four terms on the right-hand side capture horizontal

advection (denoted as HADV), vertical advection (denoted as VADV), eddy advection (denoted as EDDY), and diabatic processes (denoted as DISS), as defined in Ma et al. (2013).

At early times, each term of Eq. (12) was integrated from 0 h to 6 h, and the budget results of the DMC and DMC–TMC simulations are shown in Fig. 9. Equation (12) was integrated forward at time steps of 60 min. The q_v tendency term in the eyewall region was nearly positive, indicating that q_v increased. Negative radial inward advection was mainly observed in the boundary inflow layer. The positive VADV term covered a large area, while the EDDY term largely attained negative values in the eyewall region. The DISS term attained considerably negative values but was approximately offset by the positive VADV term. Compared to the TMC simulation, q_v vertical advection in the eye region at altitudes from 900 hPa to 350 hPa, in the eyewall region at an altitude of 600 hPa and in the boundary inflow layer was lower in the DMC simulation, while q_v vertical advection in the eyewall region at altitudes from 950 hPa to 450 hPa was largely higher in the DMC simulation. The differences in the HADV and EDDY terms between the DMC and TMC simulations were almost the same. Since the primary differences in q_v were smaller in the boundary inflow layer and in the eye region at altitudes from 900 hPa to 300 hPa and larger in the eyewall region at altitudes from 950 hPa to 500 hPa, by examining the q_v tendency due to each term from 0–6 h, the results indicated that vertical advection played a major role.

From 42–48 h, radial inward advection, upward advection, and the DISS term became much stronger in the DMC simulation, especially the VADV term. Similar to the 0–6-h forecast periods, the VADV term was responsible for the positive tangential q_v tendency and the differences between the DMC and TMC simulations (Fig. 10).

The VADV term difference between the DMC and TMC simulations at 6 h and 48 h is shown in Fig. 11. The difference in the VADV term was similar to that in $\overline{w}$
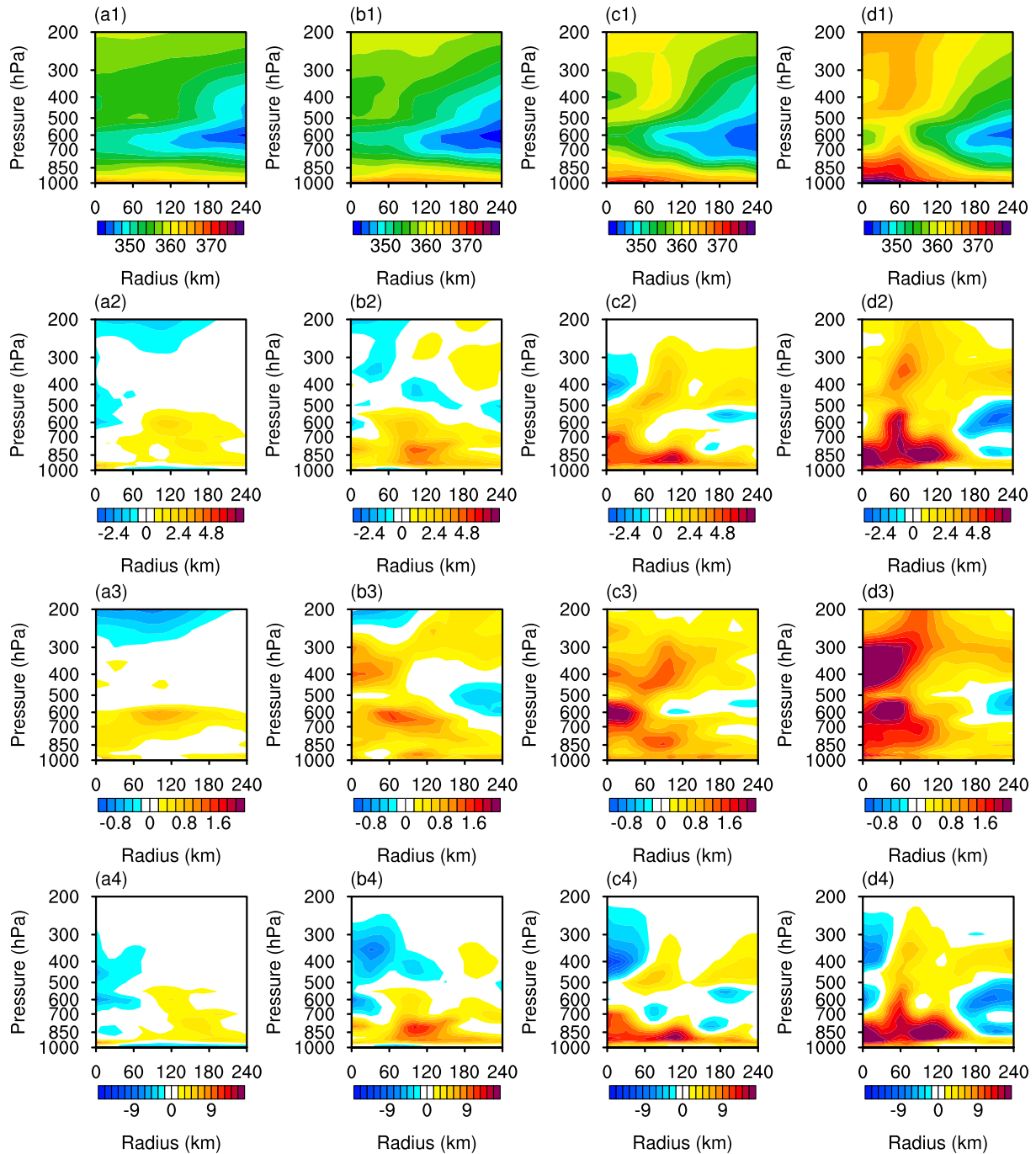
Fig. 7. Height–radius cross sections of the temporally and azimuthally averaged EPT (K) in (a1–d1) the DMC simulation at 6 h (a1), 12 h (b1), 24 h (c1), and 48 h (d1). (a2–d2) are the same as (a1–d1) but for the DMC–TMC, (a3–d3) are the same as (a2–d2) but for the average temperature (K), and (a4–d4) are the same as (a3–d3) but for the average water vapor mixing ratio (10^{-4} g kg^{-1}).

(Figs. 12a and 12d), and the differences in the VADV term were mainly determined by $\bar{w}$. These results suggested that the moister area in the eyewall region (drier boundary inflow layer at early times) determined in the DMC simulation was probably the result of enhanced (inhibited) updraft.

4.5.   *Vertical velocity and rainbands*

The significant difference between the DMC and TMC dynamical cores is the change in total water in the continuity equation. The full pressure vertical velocity and surface pressure tendency equations in the DMC dynamical core include another term associated with the total water, as mentioned in section 2.3. However, there was no difference in the surface pressure at early times (Fig. 2b), but the air in the DMC simulation was warmer and moister than that in the TMC simulation (Fig. 7). Water vapor mixing ratio budget
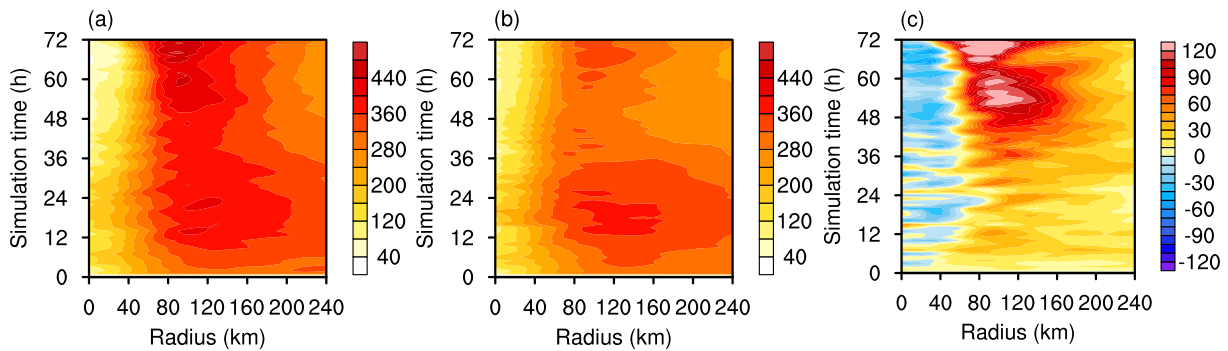
Fig. 8. Hovmöller diagram of the azimuthally averaged SLHF (W m^{-2}) in the (a) DMC, (b) TMC, and (c) DMC–TMC simulations.

analysis indicated that vertical motion played a major role. In addition, rainbands impose critical effects on TC intensity changes (Wang and Wu, 2004; Li and Wang, 2012; Li et al., 2014; Hendricks et al., 2019; Tang et al., 2020). Therefore, the TC vertical velocity and rainbands are further examined to explain the pronounced improvement in TC intensity forecasts using the DMC dynamical core in this section.

Azimuthal-mean cross sections of vertical motion and the azimuthal-mean two-hourly surface rain rate simulated with the DMC dynamical core at the different times are shown in Fig. 13. It is evident that the upward motion in the eyewall region increased over time, as shown in Fig. 4. The surface rain rate was clearly a response to the upward motion in the eyewall region and inner rainbands. The heaviest precipitation occurred at the location of the maximum vertical velocity in the inner rainbands. At the early time (6 h), although the surface rain rate in the eyewall region was slightly higher in the DMC simulation (Fig. 12a), the vertical velocity in the eyewall region was higher in the DMC simulation. Upward motion facilitated the release of latent heat, thereby playing an accelerating role in the growth of the inner rainbands. As a result, the vertical velocity in the DMC simulation increasingly exceeded that in the TMC simulation, and the surface rain rate in the eyewall region increased over time (Figs. 12, 14, and 15). The higher surface rain rate inside the inner rainbands in the DMC simulation (Figs. 12, 14, 15, and 16) suggested higher net internal atmospheric diabatic heating within the inner core (Wang, 2009), as the average perturbation temperature was higher in the DMC simulation than in the TMC simulation (Fig. 6). Internal atmospheric diabatic heating could warm the atmospheric column and lower the surface pressure (Wang, 2009). Therefore, the higher inner rainband heating in the DMC simulation could increase the pressure gradient across the RMW (Fig. 16), requiring a stronger tangential wind to balance and thus produce a stronger TC intensity (Figs. 2b and c).

5.　Conclusions and discussion

In this study, the TC simulation performance of a DMC hydrostatic global spectral dynamical core (the DMC dynamical core) was investigated and compared to that of a total

(moist) mass conserving dynamical core (the TMC dynamical core). The TC forecasts were first evaluated against 20 TCs observed in the West Pacific region during the 2020 typhoon season. To better understand the impacts of the DMC dynamical core on TC position and intensity prediction, one TC case was examined.

As expected, both the tracks and intensities were improved with the DMC dynamical core. However, the improvement in the intensity forecasts was much greater than that in the TC track forecasts, with the TC track forecast error reduction being no more than 7% and the intensity forecast error reduction being at least 17% for all TCs. In the three intensity classifications, the track errors of the DMC dynamical core indicated the largest deterioration of 18.5% in the tropical storm intensity at 120 h, while the intensity forecast errors of the DMC dynamical core indicated the smallest reduction of 12.8% in the tropical storm intensity.

The distinct differences in the TC intensity, track, and structure between the DMC and TMC dynamical cores were consistent with those reported in a previous study of idealized TC test cases (Peng et al., 2020). Although the TC tracks slightly differed for the later forecast lead time, with both simulations yielding tracks largely coinciding with the observed tracks, the predicted TC tracks for the early forecast lead time obtained with the DMC dynamical core exhibited smaller absolute errors than those obtained with the TMC dynamical core. The TC intensity produced with the DMC dynamical core was higher for all forecast lead times and much closer to the observed TC intensity. In general, the DMC dynamical core was important in model development for TC forecasting purposes, especially to improve the predicted TC intensity.

The DMC dynamical core also profoundly impacted the storm structures. The three-dimensional winds, warm cores, and moist cores were consistently enhanced with the storm intensity. At early simulation times (0–6 h), although the minimum SLP in the DMC simulation matched that in the TMC simulation, the air above the boundary layer and in the boundary inflow layer contributed to notably positive and negative moisture differences, respectively, and the eyewall air in the DMC simulation above the boundary layer was warmer and moister. As the storm developed, the DMC
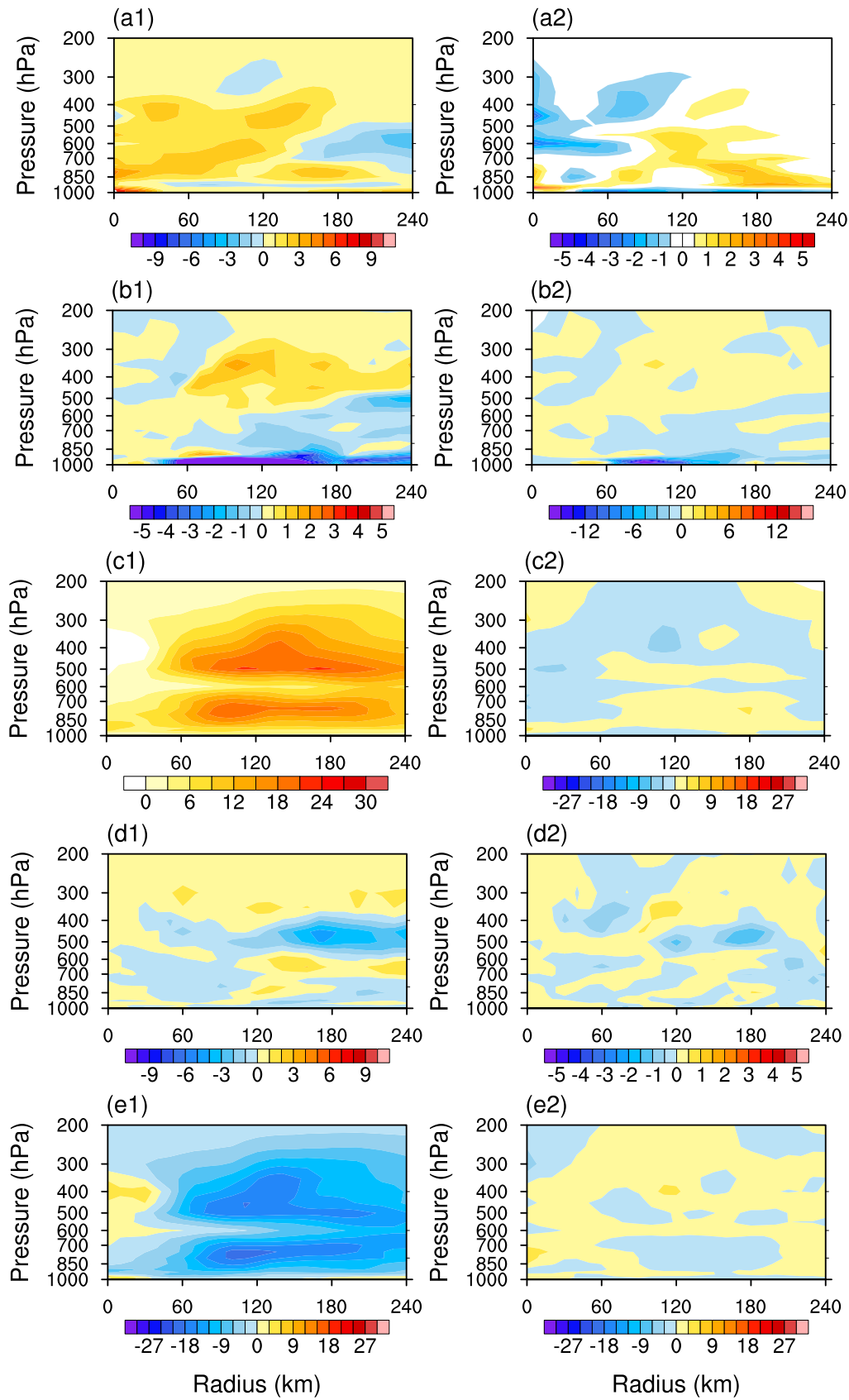
Fig. 9. Time-integrated azimuthal-mean tangential q_v tendency terms (10^{-8} s^{-1}) of Eq. (12) from 0 h to 6 h. Temporal integration of (a1, a2) the tangential q_v tendency in the model simulations, (b1, b2) the HADV term, (c1, c2) the VADV term, (d1, d2) the EDDY term, and (e1, e2) the DISS term in the (a1–e1) DMC and (a2–e2) DMC–TMC simulations.
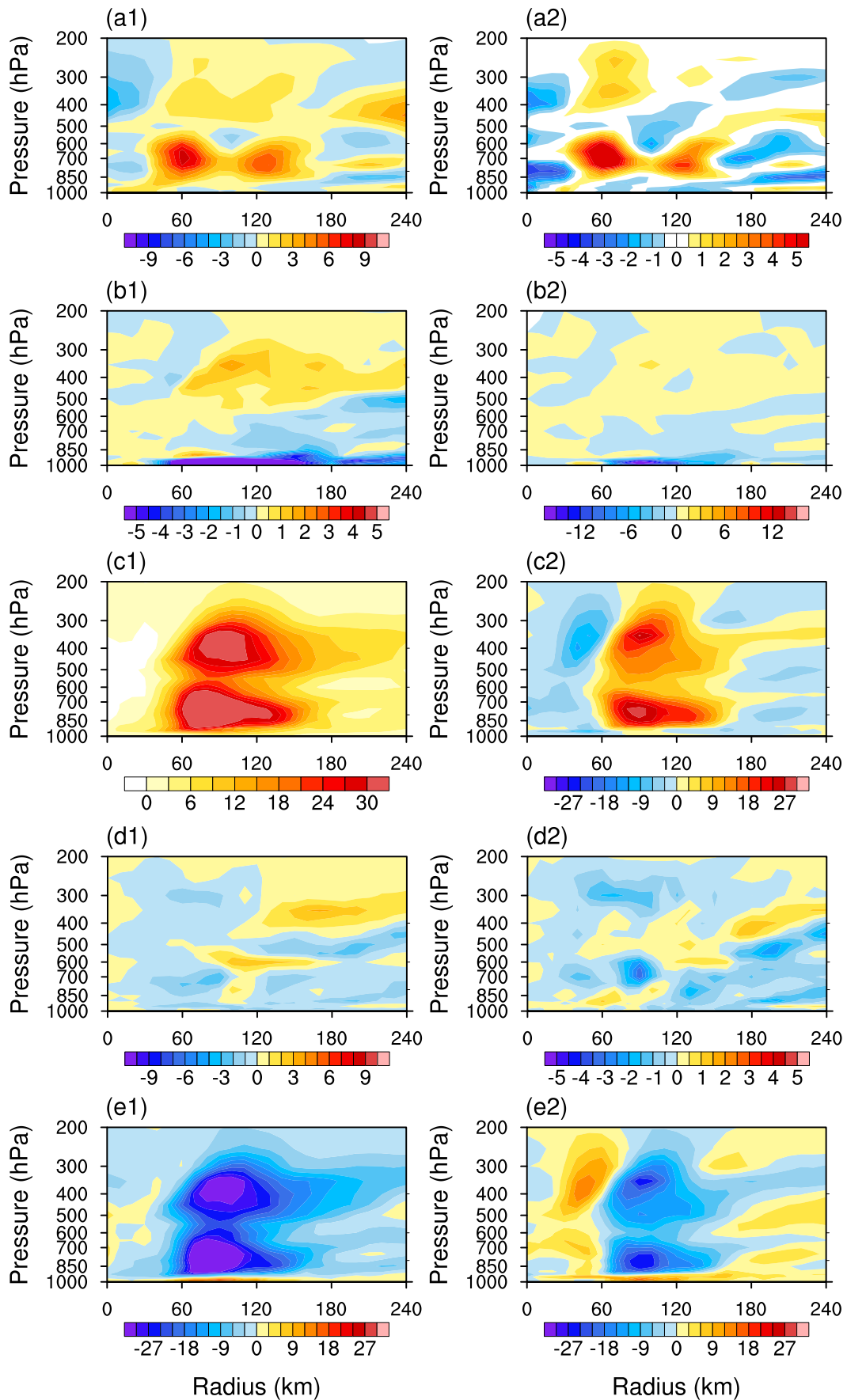
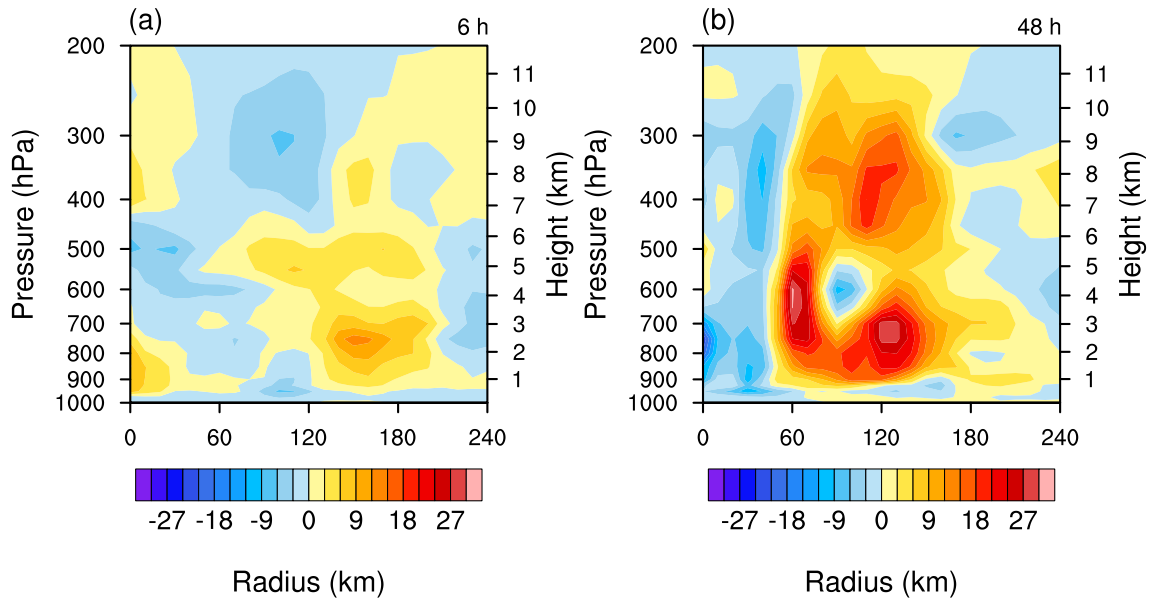**Fig. 10.** Same as in Fig. 9 but from 42–48 h.

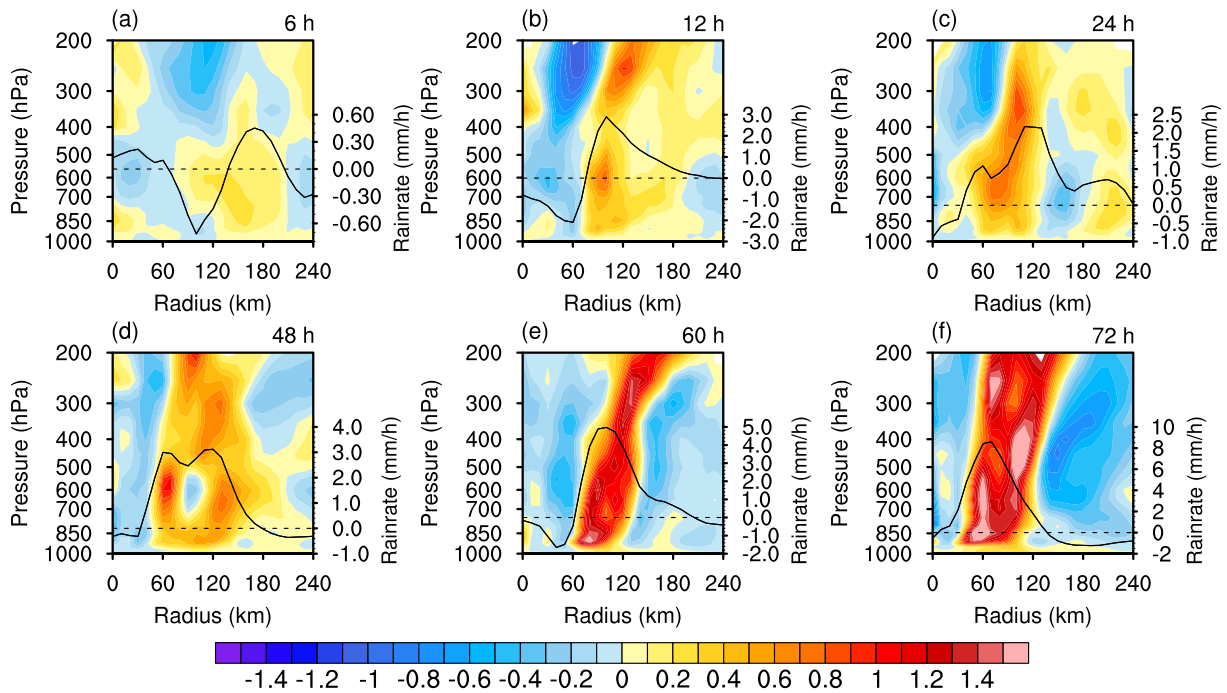**Fig. 11.** VADV in the DMC–TMC simulation at (a) 6 h and (b) 48 h.

Fig. 12. Radial vertical structure of the azimuthal-mean vertical motion (hPa s^{-1}; shading; left legend) at the top of each panel and the azimuthal-mean surface rain rate (mm h^{-1}; solid curves; right legend) averaged between $t-1$ and $t+1$ h (t=6, 12, 24, 48, 60, and 72 h) in the DMC-TMC simulation. The dashed line in each panel denotes the 0 mm h^{-1} surface rain rate.

simulation yielded a lower minimum SLP, and the eyewall air in the DMC simulation became much warmer and moister. The azimuthal-mean tangential water vapor mixing ratio tendency budget was calculated to explore the possible reasons for this result. The vertical advection process was identified as playing a key role. As a result, more upward-moving moist air originating from the low-level region was transported into the higher troposphere, and the updraft-induced adiabatic warming was consequently enhanced; there-

fore, the eyewall air above the boundary level was moister and warmer. The drier boundary layer simulated by the DMC dynamical core at an early time, leading to an increase in the SLHF, the major energy source of TC intensification, was mainly caused by the increased updraft above the boundary level. In addition, the surface rain rate represented a response to upward motion. The surface rain rate in the eyewall region was higher in the DMC simulation, as the vertical velocity in the DMC simulation was higher than
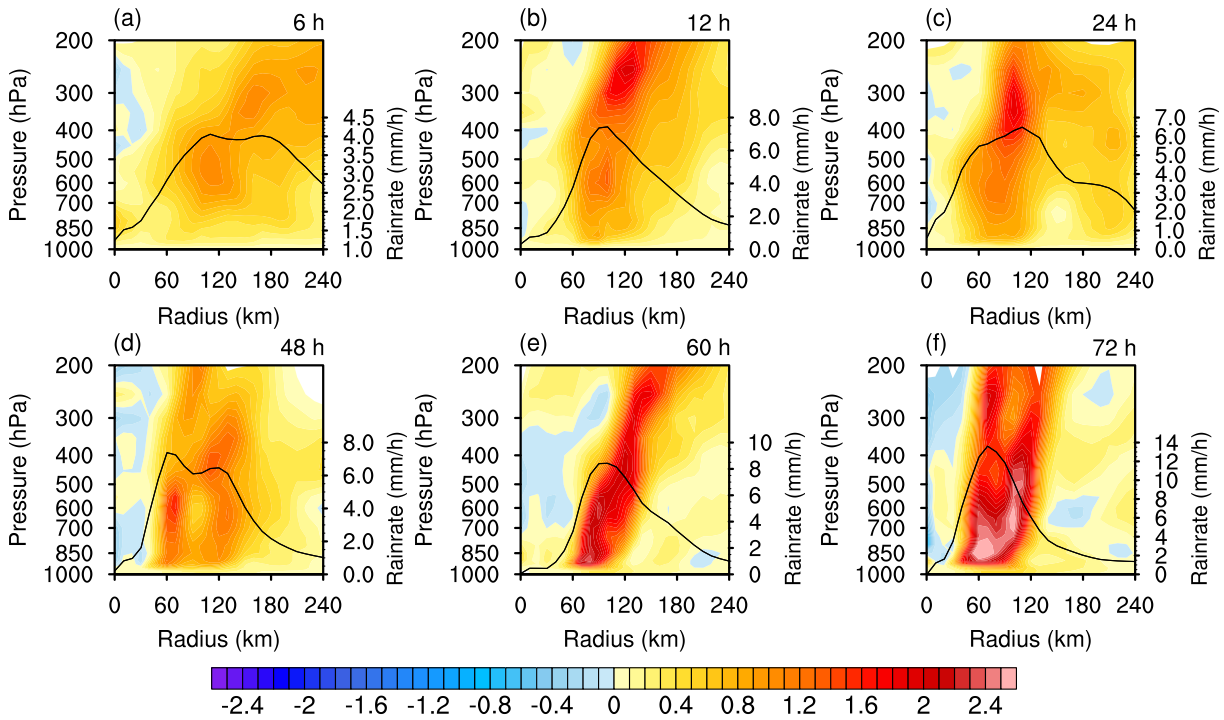
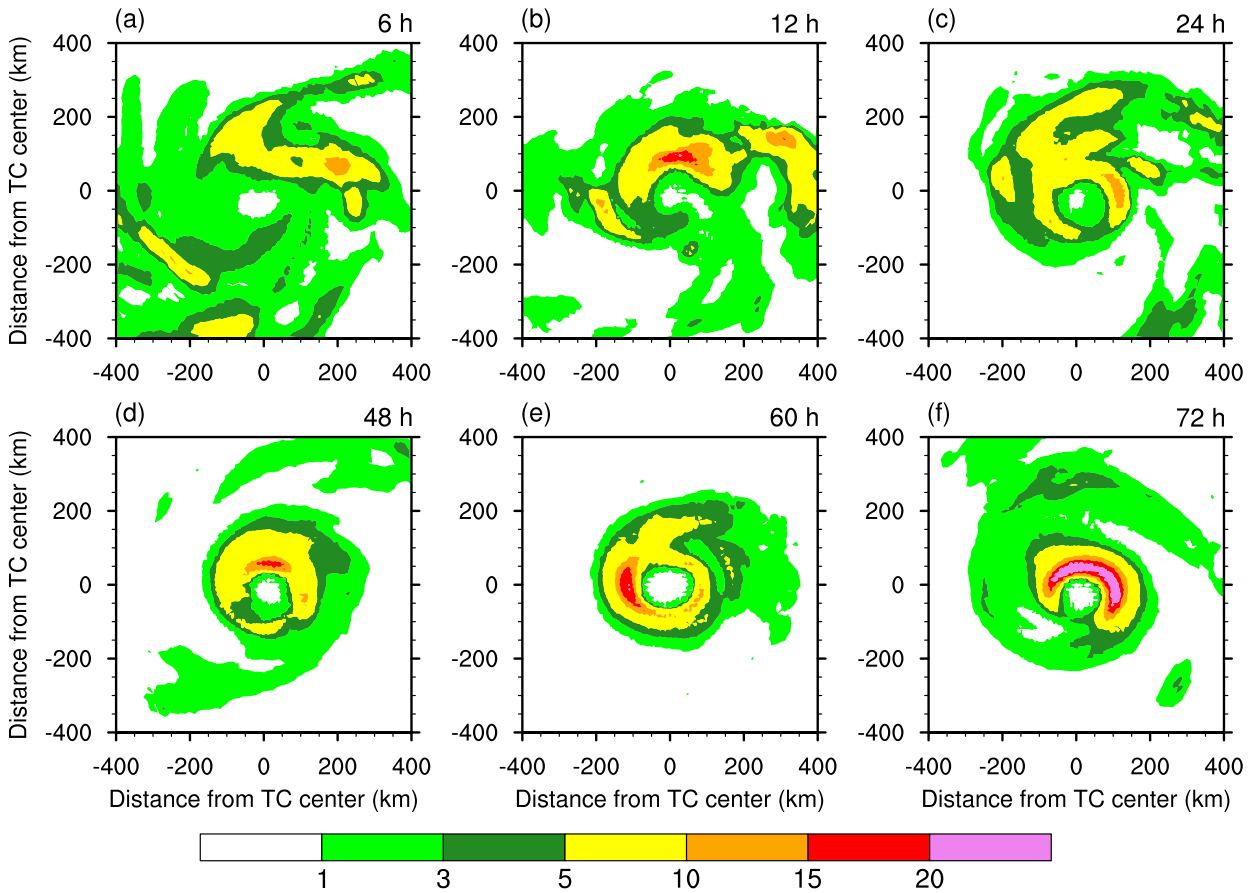**Fig. 13.** Same as in Fig. 12, but for the DMC simulation.

Fig. 14. Distribution of the hourly precipitation (mm) at the simulation time given at the top of each panel in the DMC simulation.
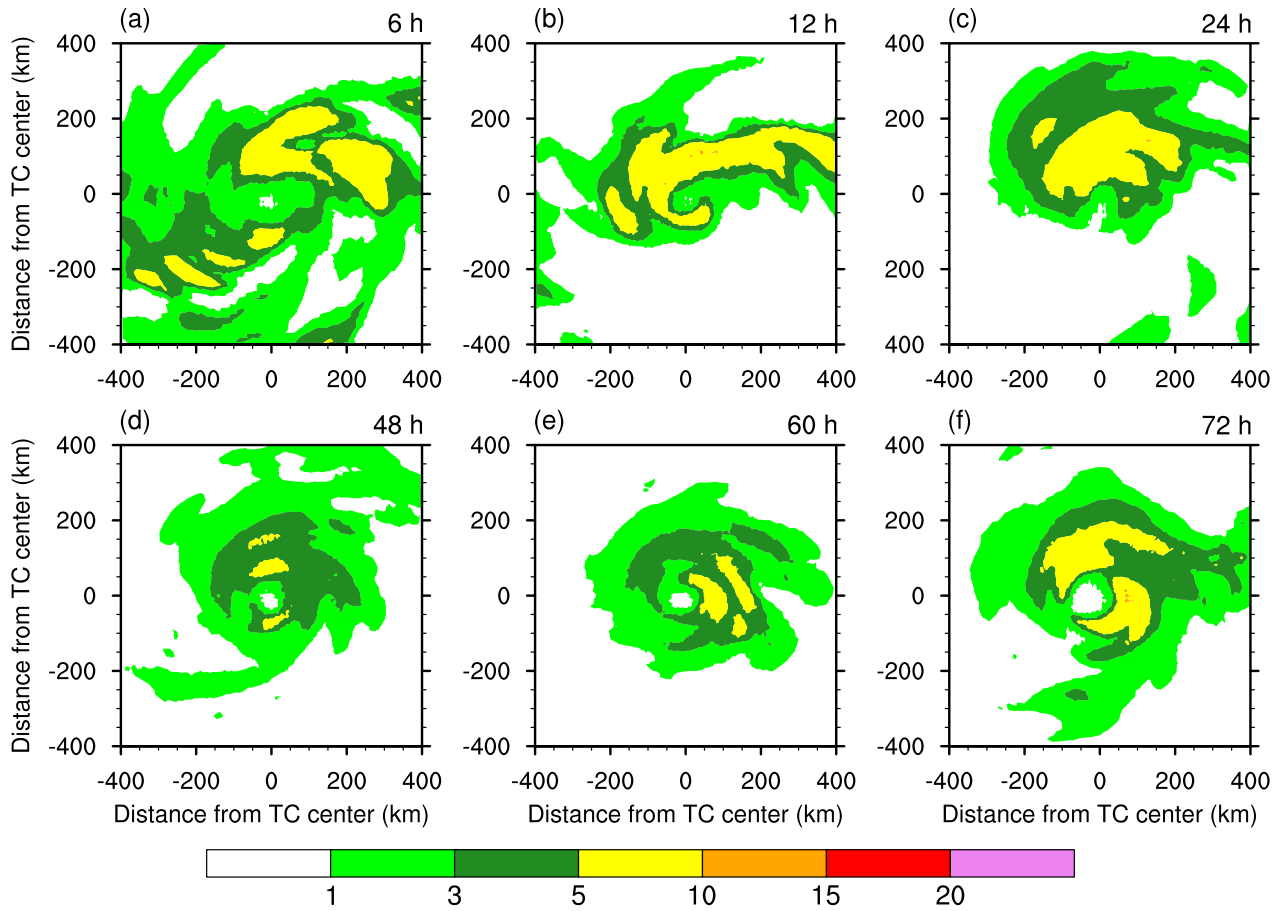
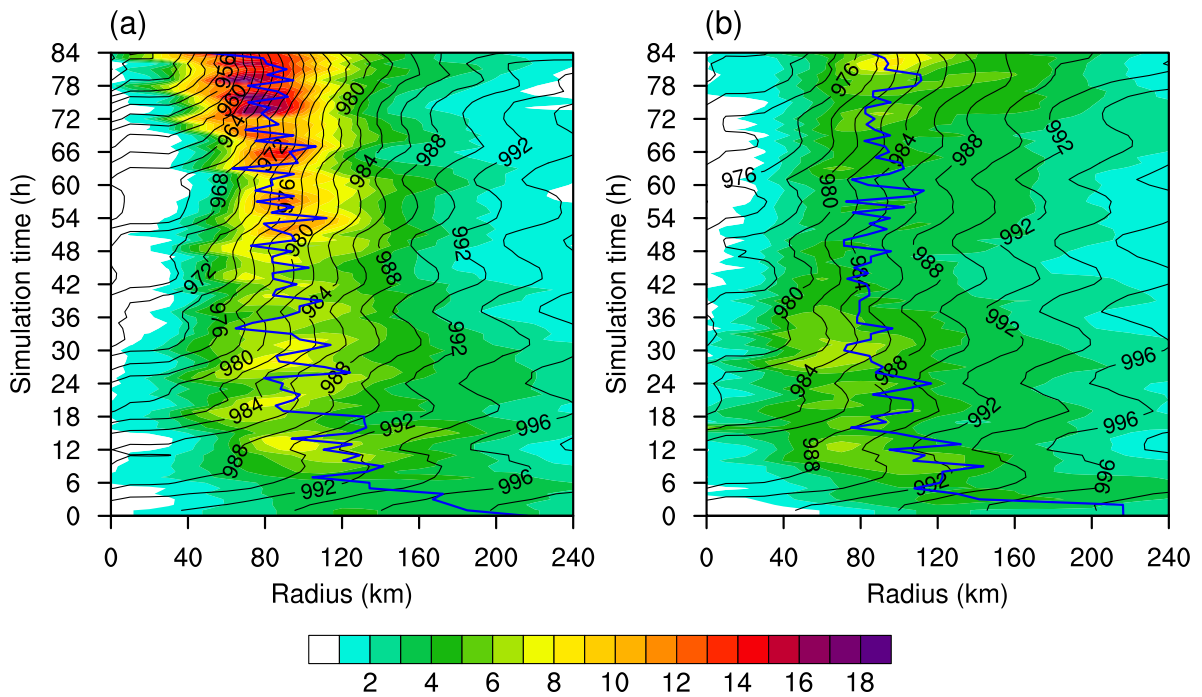**Fig. 15.** Same as in Fig. 14, but for the TMC simulation.

Fig. 16. Radius–time Hovmöller diagrams of the azimuthal-mean hourly precipitation (mm; shading) and mean surface pressure (hPa; contours) with contour intervals of 2 hPa based on the hourly model outputs of the (a) DMC and (b) TMC experiments. The blue lines denote the RMW.

that in the TMC simulation. The higher surface rain rate within the inner rainbands in the DMC simulation indicated higher net internal atmospheric diabatic heating inside the inner core, which could warm the atmospheric column and lower the surface pressure (Wang, 2009). Therefore, the pressure gradient across the RMW increased, and the tangential winds also increased and thus produced a stronger TC intensity.

These results indicated that the change in total water in the dynamical core was not negligible and exerted a notable effect on TC deepening. Although both the full pressure vertical velocity and surface pressure tendency equations in the DMC dynamical core include an additional term associated with the total water, the minimum SLP in the DMC simulation matched that in the TMC simulation from 0–6 h, but the DMC simulation yielded warmer and moister cores than the TMC simulation. The water vapor mixing ratio budget analysis results revealed that the vertical velocity played a major role. In addition, the vertical velocity and surface rain rate (net internal atmospheric diabatic heating) in the eyewall region were higher in the DMC simulation than in the TMC simulation. Internal atmospheric diabatic heating in the inner rainbands could increase the intensity. Therefore, the stronger TC intensity in the DMC simulation could be attributed to vertical motion.

Nevertheless, this work only focused on the performance of the DMC dynamical core in TC simulation. The DMC dynamical core improved TC forecasts, especially the TC intensity. The performance of the DMC dynamical core in heavy rain event forecasting should be investigated.

REFERENCES

Bauer, P., A. Thorpe, and G. Brunet, 2015: The quiet revolution of numerical weather prediction. *Nature*, **525**, 47−55, https://doi.org/10.1038/nature14956.

Biswas, M. K., and Coauthors, 2018: GFDL Vortex Tracker Users' Guide V3.9a, 35 pp.

Bloemendaal, N., S. Muis, R. J. Haarsma, M. Verlaan, M. Irazoqui Apecechea, H. De Moel, P. J. Ward, and J. C. J. H. Aerts, 2019: Global modeling of tropical cyclone storm surges using high-resolution forecasts. *Climate Dyn.*, **52**, 5031−5044, https://doi.org/10.1007/s00382-018-4430-x.

Bolton, D., 1980: The computation of equivalent potential temperature. *Mon. Wea. Rev.*, **108**, 1046−1053, https://doi.org/10.1175/1520-0493(1980)108<1046:TCOEPT>2.0.CO;2.

Bott, A., 2008: Theoretical considerations on the mass and energy consistent treatment of precipitation in cloudy atmospheres. *Atmospheric Research*, **89**, 262−269, https://doi.org/10.1016/j.atmosres.2008.02.010.

Bretherton, C. S., and S. Park, 2009: A new moist turbulence parameterization in the community atmosphere model. *J. Cli-

mat*e, **22**, 3422−3448, https://doi.org/10.1175/2008JCLI2556.1.

Byun, D. W., 1999: Dynamically consistent formulations in meteorological and air quality models for multiscale atmospheric studies. Part I: Governing equations in a generalized coordinate system. *J. Atmos. Sci.*, **56**, 3789−3807, https://doi.org/10.1175/1520-0469(1999)056<3789:DCFIMA>2.0.CO;2.

Cangialosi, J. P., E. Blake, M. Demaria, A. Penny, A. Latto, E. Rappaport, and V. Tallapragada, 2020: Recent progress in tropical cyclone intensity forecasting at the national hurricane center. *Wea. Forecasting*, **35**, 1913−1922, https://doi.org/10.1175/WAF-D-20-0059.1.

Dudhia, J., 2014: A history of mesoscale model development. *Asia-Pacific Journal of Atmospheric Sciences*, **50**, 121−131, https://doi.org/10.1007/s13143-014-0031-8.

Emanuel, K., 2000: A statistical analysis of tropical cyclone intensity. *Mon. Wea. Rev.*, **128**, 1139−1152, https://doi.org/10.1175/1520-0493(2000)128<1139:ASAOTC>2.0.CO;2.

Emanuel, K., C. DesAutels, C. Holloway, and R. Korty, 2004: Environmental control of tropical cyclone intensity. *J. Atmos. Sci.*, **61**, 843−858, https://doi.org/10.1175/1520-0469(2004)061<0843:ECOTCI>2.0.CO;2.

Forbes, R., and A. Tompkins, 2011: An improved representation of cloud and precipitation. ECMWF Newsletter, No. 129, 6 pp, https://doi.org/10.21957/nfgulzhe.

Forbes, R., A. M. Tompkins, and A. Untch, 2011: A new prognostic bulk microphysics scheme for the IFS. ECMWF Technical Memoranda, No. 649, 28 pp. https://doi.org/10.21957/bf6vjvxk.

Gu, H. D., and Z. A. Qian, 1991: A discussion about the role of the water vapor source/sink term in continuity equation of numerical models. *Chin. Sci. Bull.*, **36**, 1291−1296, https://doi.org/10.1360/csb1991-36-17-1291.

Hendricks, E. A., S. A. Braun, J. L. Vigh, and J. B. Courtney, 2019: A summary of research advances on tropical cyclone intensity change from 2014−2018. *Tropical Cyclone Research and Review*, **8**(4), 219−225, https://doi.org/10.1016/j.tcrr.2020.01.002.

Hong, S.-Y., J. Dudhia, and S.-H. Chen, 2004: A revised approach to ice microphysical processes for the bulk parameterization of clouds and precipitation. *Mon. Wea. Rev.*, **132**, 103−120, https://doi.org/10.1175/1520-0493(2004)132<0103:ARATIM>2.0.CO;2.

Iacono, M. J., J. S. Delamere, E. J. Mlawer, M. W. Shephard, S. A. Clough, and W. D. Collins, 2008: Radiative forcing by long-lived greenhouse gases: Calculations with the AER radiative transfer models. *J. Geophys. Res.*, **113**, D13103, https://doi.org/10.1029/2008JD009944.

Lackmann, G. M., and R. M. Yablonsky, 2004: The importance of the precipitation mass sink in tropical cyclones and other heavily precipitating systems. *J. Atmos. Sci.*, **61**, 1674−1692, https://doi.org/10.1175/1520-0469(2004)061<1674:TIOTPM>2.0.CO;2.

Lauritzen, P. H., and Coauthors, 2018: NCAR release of CAM-SE in CESM2.0: A reformulation of the spectral element dynamical core in dry-mass vertical coordinates with comprehensive treatment of condensates and energy. *Journal of Advances in Modeling Earth Systems*, **10**, 1537−1570, https://doi.org/10.1029/2017MS001257.

Li, Q. Q., and Y. Q. Wang, 2012: A comparison of inner and outer spiral rainbands in a numerically simulated tropical

cyclone. *Mon. Wea. Rev.*, **140**(9), 2782–2805, https://doi.org/10.1175/MWR-D-11-00237.1.

Li, Q. Q., Y. Q. Wang, and Y. H. Duan, 2014: Effects of Diabatic heating and cooling in the rapid Filamentation zone on structure and intensity of a simulated tropical cyclone. *J. Atmos. Sci.*, **71**(9), 3144–3163, https://doi.org/10.1175/JAS-D-13-0312.1.

Li, Q. Q., Y. Q. Wang, and Y. H. Duan, 2015: Impacts of evaporation of rainwater on tropical cyclone structure and intensity—A revisit. *J. Atmos. Sci.*, **72**, 1323–1345, https://doi.org/10.1175/JAS-D-14-0224.1.

Lorenz, E. N., 1960: Maximum simplification of the dynamic equations. *Tellus*, **12**, 243–254, https://doi.org/10.1111/j.2153-3490.1960.tb01307.x.

Lu, X. Q., H. Yu, M. Ying, B. K. Zhao, S. Zhang, L. M. Lin, L. N. Bai, and R. J. Wan, 2021: Western North Pacific tropical cyclone database created by the China meteorological administration. *Adv. Atmos. Sci.*, **38**, 690–699, https://doi.org/10.1007/s00376-020-0211-7.

Ma, Z. H., J. F. Fei, L. Liu, X. G. Huang, and X. P. Cheng, 2013: Effects of the cold core eddy on tropical cyclone intensity and structure under idealized Air–Sea interaction conditions. *Mon. Wea. Rev.*, **141**, 1285–1303, https://doi.org/10.1175/MWR-D-12-00123.1.

Ma, Z. H., J. F. Fei, X. G. Huang, and X. P. Cheng, 2015: Contributions of surface sensible heat fluxes to tropical cyclone. Part I: Evolution of tropical cyclone intensity and structure. *J. Atmos. Sci.*, **72**, 120–140, https://doi.org/10.1175/JAS-D-14-0199.1.

Malardel, S., M. A. Diamantakis, A. Panareda, and J. Flemming, 2019: Dry mass versus total mass conservation in the IFS. ECMWF Technical Memorandum, No. 849, 19 pp, https://doi.org/10.21957/s3ho2aq29.

Marchok, T., 2021: Important factors in the tracking of tropical cyclones in operational models. *J. Appl. Meteor. Climatol.*, **60**(9), 1265–1284, https://doi.org/10.1175/JAMC-D-20-0175.1.

Mlawer, E. J., S. J. Taubman, P. D. Brown, M. J. Iacono, and S. A. Clough, 1997: Radiative transfer for inhomogeneous atmospheres: RRTM, a validated correlated-k model for the longwave. *J. Geophys. Res.*, **102**(D14), 16 663–16 682, https://doi.org/10.1029/97JD00237.

Neale, R. B., and Coauthors, 2012: Description of the NCAR community atmosphere model (CAM 5.0). NCAR Technical Note NCAR/TN-486+STR, 274 pp, https://doi.org/10.5065/wgtk-4g06.

Peng, J., J. P. Wu, W. M. Zhang, J. Zhao, L. F. Zhang, and J. H. Yang, 2019: A modified nonhydrostatic moist global spectral dynamical core using a dry-mass vertical coordinate. *Quart. J. Roy. Meteor. Soc.*, **145**, 2477–2490, https://doi.org/10.1002/qj.3574.

Peng, J., J. Zhao, W. M. Zhang, L. F. Zhang, J. P. Wu, and X. R. Yang, 2020: Towards a dry-mass conserving hydrostatic global spectral dynamical core in a general moist atmosphere. *Quart. J. Roy. Meteor. Soc.*, **146**, 3206–3224, https://doi.org/10.1002/qj.3842.

Qiu, C.-J., J.-W. Bao, and Q. Xu, 1993: Is the mass sink due to precipitation negligible. *Mon. Wea. Rev.*, **121**, 853–857, https://doi.org/10.1175/1520-0493(1993)121<0853:ITMSDT>2.0.CO;2.

Rogers, R. F., 2021: Recent advances in our understanding of tropical cyclone intensity change processes from airborne observa-

tions. *Atmosphere*, **12**, 650, https://doi.org/10.3390/atmos12050650.

Schaffer, J. D., P. J. Roebber, and C. Evans, 2020: Development and evaluation of an evolutionary programming-based tropical cyclone intensity model. *Mon. Wea. Rev.*, **148**, 1951–1970, https://doi.org/10.1175/MWR-D-19-0346.1.

Stern, D. P., and D. S. Nolan, 2012: On the height of the warm core in tropical cyclones. *J. Atmos. Sci.*, **69**, 1657–1680, https://doi.org/10.1175/JAS-D-11-010.1.

Sun, J., H. L. He, X. M. Hu, D. Q. Wang, C. Gao, and J. B. Song, 2019: Numerical simulations of typhoon Hagupit (2008) using WRF. *Wea. Forecasting*, **34**, 999–1015, https://doi.org/10.1175/WAF-D-18-0150.1.

Tang, B. H., and Coauthors, 2020: Recent advances in research on tropical cyclogenesis. *Tropical Cyclone Research and Review*, **9**(2), 87–105, https://doi.org/10.1016/j.tcrr.2020.04.004.

Vigh, J. L., and Coauthors, 2018: Tropical Cyclone Intensity Change: Internal Influences. Rapporteur Report, Topic 3.1., *Ninth International Workshop on Tropical Cyclones (IWTC-IX)*, Honolulu, Hawaii.

Wang, C. X., Z. H. Zeng, and M. Ying, 2020: Uncertainty in tropical cyclone intensity predictions due to uncertainty in initial conditions. *Adv. Atmos. Sci.*, **37**(3), 278–290, https://doi.org/10.1007/s00376-019-9126-6.

Wang, Y. Q., 2009: How do outer spiral Rainbands affect tropical cyclone structure and intensity. *J. Atmos. Sci*, **66**(5), 1250–1273, https://doi.org/10.1175/2008JAS2737.1.

Wang, Y. Q., and C. C. Wu, 2004: Current understanding of tropical cyclone structure and intensity changes−A review. *Meteorol. Atmos. Phys.*, **87**(4), 257–278, https://doi.org/10.1007/s00703-003-0055-6.

Wang, Y. Q., and J. Xu, 2010: Energy production, frictional dissipation, and maximum intensity of a numerically simulated tropical cyclone. *J. Atmos. Sci.*, **67**, 97–116, https://doi.org/10.1175/2009JAS3143.1.

Wedi, N., and Coauthors, 2015: The modelling infrastructure of the integrated forecasting system: Recent advances and future challenges. ECMWF Technical Memorandum, No. 760, 48 pp, https://doi.org/10.21957/thtpwp67e.

Wu, J. P., J. Zhao, J. Q. Song, and W. M. Zhang, 2011: Preliminary design of dynamic framework for global non-hydrostatic spectral model. *Computer Engineering and Design*, **32**, 3539–3543, https://doi.org/10.16208/j.issn1000-7024.2011.10.001. (in Chinese with English abstract)

Yan, Q., T. Wei, R. L. Korty, J. P. Kossin, Z. S. Zhang, and H. J. Wang, 2016: Enhanced intensity of global tropical cyclones during the mid-Pliocene warm period. *Proceedings of the National Academy of Sciences of the United States of America*, **113**, 12 963–12 967, https://doi.org/10.1073/pnas.1608950113.

Yang, J. H., J. Q. Song, J. P. Wu, F. K. Ying, J. Peng, and H. Z. Leng, 2017: A semi-implicit deep-atmosphere spectral dynamical kernel using a hydrostatic-pressure coordinate. *Quart. J. Roy. Meteor. Soc.*, **143**, 2703–2713, https://doi.org/10.1002/qj.3119.

Yin, F. K., G. L. Wu, J. P. Wu, J. Zhao, and J. Q. Song, 2018: Performance evaluation of the fast spherical harmonic transform algorithm in the Yin-He global spectral model. *Mon. Wea. Rev.*, **146**, 3163–3182, https://doi.org/10.1175/MWR-D-18-0151.1.

Yin, F. K., J. Q. Song, J. P. Wu, and W. M. Zhang, 2021: An imple-

mentation of single-precision fast spherical harmonic transform in Yin-He global spectral model. *Quart. J. Roy. Meteor. Soc.*, **147**, 2323–2334, https://doi.org/10.1002/qj.4026.

Ying, M., W. Zhang, H. Yu, X. Q. Lu, J. X. Feng, Y. X. Fan, Y. T. Zhu, and D. Q. Chen, 2014: An overview of the China meteorological administration tropical cyclone database. *J.* *Atmos. Oceanic Technol.*, **31**, 287–301, https://doi.org/10.1175/JTECH-D-12-00119.1.

Zhang, C. X., and Y. Q. Wang, 2017: Projected future changes of tropical cyclone activity over the Western North and South Pacific in a 20-km-mesh regional climate model. *J. Climate*, **30**, 5923–5941, https://doi.org/10.1175/JCLI-D-16-0597.1.